# Energy dependence of $\phi$ meson production in central Pb+Pb collisions at $\sqrt{s_{NN}} = 6$ to 17 GeV

C. Alt,[9] T. Anticic,[23] B. Baatar,[8] D. Barna,[4] J. Bartke,[6] L. Betev,[10] H. Białkowska,[20] C. Blume,[9] B. Boimska,[20] M. Botje,[1] J. Bracinik,[3] R. Bramm,[7] P. Buncic,[10] V. Cerny,[3] P. Christakoglou,[2] P. Chung,[19] O. Chvala,[14] J. G. Cramer,[16] P. Csató,[4] P. Dinkelaker,[9] V. Eckardt,[13] D. Flierl,[9] Z. Fodor,[4] P. Foka,[7] V. Friese,[7] J. Gál,[4] M. Gaździcki,[9,11] V. Genchev,[18] G. Georgopoulos,[2] E. Gładysz,[6] K. Grebieszkow,[22] S. Hegyi,[4] C. Höhne,[7] K. Kadija,[23] A. Karev,[13] D. Kikola,[22] M. Kliemant,[9] S. Kniege,[9] V. I. Kolesnikov,[8] T. Kollegger,[9] E. Kornas,[6] R. Korus,[11] M. Kowalski,[6] I. Kraus,[7] M. Kreps,[3] D. Kresan,[7] A. Laszlo,[4] R. Lacey,[19] M. van Leeuwen,[1] P. Lévai,[4] L. Litov,[17] B. Lungwitz,[9] M. Makariev,[17] A. I. Malakhov,[8] M. Mateev,[17] G. L. Melkumov,[8] A. Mischke,[1] M. Mitrovski,[9] J. Molnár,[4] St. Mrówczyński,[11] V. Nicolic,[23] G. Pálla,[4] A. D. Panagiotou,[2] D. Panayotov,[17] A. Petridis,[2,*] W. Peryt,[22] M. Pikna,[3] J. Pluta,[22] D. Prindle,[16] F. Pühlhofer,[12] R. Renfordt,[9] C. Roland,[5] G. Roland,[5] M. Rybczyński,[11] A. Rybicki,[6] A. Sandoval,[7] N. Schmitz,[13] T. Schuster,[9] P. Seyboth,[13] F. Siklér,[4] B. Sitar,[3] E. Skrzypczak,[21] M. Slodkowski,[22] G. Stefanek,[11] R. Stock,[9] C. Strabel,[9] H. Ströbele,[9] T. Susa,[23] I. Szentpétery,[4] J. Sziklai,[4] M. Szuba,[22] P. Szymanski,[20] V. Trubnikov,[20] D. Varga,[4] M. Vassiliou,[2] G. I. Veres,[4] G. Vesztergombi,[4] D. Vranić,[7] A. Wetzler,[9] Z. Włodarczyk,[11] I. K. Yoo,[15] and J. Zimányi[4,*]

(NA49 Collaboration)

[1] *NIKHEF, Amsterdam, Netherlands*
[2] *Department of Physics, University of Athens, Athens, Greece*
[3] *Comenius University, Bratislava, Slovakia*
[4] *KFKI Research Institute for Particle and Nuclear Physics, Budapest, Hungary*
[5] *MIT, Cambridge, Massachusetts, USA*
[6] *Henryk Niewodniczanski Institute of Nuclear Physics, Polish Academy of Science, Cracow, Poland*
[7] *Gesellschaft für Schwerionenforschung (GSI), Darmstadt, Germany*
[8] *Joint Institute for Nuclear Research, Dubna, Russia*
[9] *Fachbereich Physik der Universität, Frankfurt, Germany*
[10] *CERN, Geneva, Switzerland*
[11] *Institute of Physics Świ etokrzyska Academy, Kielce, Poland*
[12] *Fachbereich Physik der Universität, Marburg, Germany*
[13] *Max-Planck-Institut für Physik, Munich, Germany*
[14] *Institute of Particle and Nuclear Physics, Charles University, Prague, Czech Republic*
[15] *Department of Physics, Pusan National University, Pusan, Republic of Korea*
[16] *Nuclear Physics Laboratory, University of Washington, Seattle, Washington, USA*
[17] *Atomic Physics Department, Sofia University St. Kliment Ohridski, Sofia, Bulgaria*
[18] *Institute for Nuclear Research and Nuclear Energy, Sofia, Bulgaria*
[19] *Department of Chemistry, Stony Brook University (SUNYSB), Stony Brook, New York, USA*
[20] *Institute for Nuclear Studies, Warsaw, Poland*
[21] *Institute for Experimental Physics, University of Warsaw, Warsaw, Poland*
[22] *Faculty of Physics, Warsaw University of Technology, Warsaw, Poland*
[23] *Rudjer Boskovic Institute, Zagreb, Croatia*

$\phi$ meson production is studied by the NA49 Collaboration in central Pb+Pb collisions at 20$A$, 30$A$, 40$A$, 80$A$, and 158$A$ GeV beam energy. The data are compared with measurements at lower and higher energies and with microscopic and thermal models. The energy dependence of yields and spectral distributions is compatible with the assumption that partonic degrees of freedom set in at low SPS energies.

## I. INTRODUCTION

The production of strange particles is considered one of the key observables for understanding the reaction mechanisms in ultrarelativistic heavy-ion collisions. Enhanced strangeness production with respect to proton-proton collisions was originally proposed as a signature of the transition to a deconfined state of quarks and gluons during the initial

*Deceased.

stage of the reactions [1]. The enhancement was predicted to arise from gluon fragmentation into quark-antiquark pairs which is believed to have a significantly lower threshold than strange-antistrange hadron pair production channels. Indeed, it has been observed [2, 3] that the ratio of the number of produced kaons to that of pions is higher by a factor of about 2 in central S + S and Pb + Pb reactions than that in $p+p$ collisions at the top energy available at the CERN Super Proton Synchroton (SPS).

Statistical hadron gas models have been successfully employed to describe the measured particle yields at various collision energies [4, 5, 6, 7, 8]. The fact that the hadronic final state of the collision resembles a hadron gas in chemical equilibrium has been interpreted as a consequence of the hadronization process [9] or as a result of a fast hadronic equilibration process involving multiparticle collisions [10]. In this hadron gas picture, enhanced production of strange particles in collisions of large nuclei arises as a consequence of the increased reaction volume, relaxing the influence of strangeness conservation [11]. Technically, this requires the application of the canonical ensemble to small collision systems, while for larger volumes such as those encountered in central collisions of heavy ions, the grand-canonical approximation is valid. It has been shown that this "canonical strangeness suppression" also applies to a partonic system [12].

In addition to this volume effect, the strange particle phase space appears to be undersaturated in elementary interactions. The deviation of the strange particle yields from a hadron gas in full equilibrium was parametrized by a strangeness undersaturation factor $\gamma_S$ [8, 13]. The additional suppression becomes much weaker in heavy-ion collisions. However, fits to the hadron multiplicities in full phase space are still unsatisfactory when not taking into account $\gamma_S$ [8]. A possible interpretation is that the total amount of strangeness available for hadronization is determined in a prehadronic stage of the collision. A change in $\gamma_S$ between $p+p$ and $A+A$ would then reflect the difference in the initial conditions of the respective fireballs.

The hadron gas model was extended to describe the energy dependence of produced hadron multiplicities by a smooth parametrization of the fit parameters $T$ and $\mu_B$, determined at energies available at the BNL Alternating Gradient Synchroton (AGS), SPS, and BNL Relativistic Heavy Ion Collider (RHIC), as a function of collision energy [14]. However, this extended model failed to reproduce the detailed features of the energy dependence of relative strangeness production measured by NA49 in its energy scan program. In particular, the sharp maximum at around 30$A$ GeV beam energy [15, 16] could not be described. The same holds true for microscopic reaction models such as UrQMD [17]. On the other hand, this feature was predicted as a consequence of the onset of a phase transition to a deconfined state at the respective beam energy [18].

In this context, it is certainly interesting to investigate specific strangeness-carrying hadrons. Among these, the $\phi$ meson is of particular interest because of its $s\overline{s}$ valence quark composition. In a purely hadronic scenario, being strangeness-neutral, it should not be sensitive to hadrochemical effects related to strangeness. If on the other hand, the amount of available strange quarks is determined in a partonic stage of the collision, the $\phi$ is expected to react more sensitively than singly strange particles. In particular, one would expect the $\phi$ meson yield to be suppressed by $\gamma_s^2$ with respect to equilibrium. Analogously, the canonical suppression mechanism in small systems should have a stronger effect on the $\phi$, leading to a larger relative enhancement in Pb + Pb collisions with respect to $p+p$ reactions than observed for kaons.

In the evolution of the fireball after hadronization, $\phi$ mesons can be both formed by kaon coalescence and destroyed by rescattering. In addition, when decaying inside the fireball, the daughter particles can rescatter, leading to a loss of signal in the invariant mass peak of the respective decay channel. This is more likely to happen for slow $\phi$ mesons, which spend more time in the fireball. Thus the effect could lead to a depletion of the $\phi$ meson yield at low $p_t$ in central nucleus-nucleus collisions [19].

Theoretical investigations have suggested that the properties of the $\phi$ meson might be modified in a dense hadronic medium. In particular, a decrease of its mass of the order of 10 MeV[1] [20] and an increase of its width by a factor of 2–3 [21] were predicted. So far, there is only one experimental claim for a broadening of the width in $p$ + Cu collisions [22].

In an earlier publication [23], we reported on $\phi$ production at top SPS energy, where we found the $\phi$ enhanced by a factor of about 3, compared to minimum bias $p+p$ collisions at the same beam energy. Meanwhile, the $\phi$ meson was measured at the same energy by the NA50 [24], NA45 [25], and NA60 [26] experiments. At the AGS, data on $\phi$ production were obtained by the E917 Collaboration in Au + Au collisions at $p_{\mathrm{beam}} = 11.7A$ GeV ($\sqrt{s_{NN}} = 4.88$ GeV) in a restricted rapidity range $[y_{\mathrm{c.m.}} - 0.4, y_{\mathrm{c.m.}}]$ [27]. At the RHIC, the STAR Collaboration measured the $\phi$ meson at $\sqrt{s_{NN}} = 130$ and $\sqrt{s_{NN}} = 200$ GeV at midrapidity [28, 29]. For the latter energy, data are also available from the PHENIX experiment [30].

In this article, we report on $\phi$ production in central Pb+Pb collisions at five different beam energies from 20$A$

[1] For better readability, we use natural units, i.e., $c = 1$, throughout this article.

TABLE I: Characteristics of the data sets employed in the analysis. The mean numbers of wounded nucleons $\langle N_w \rangle$ were obtained by Glauber model calculations.

| $E_{\mathrm{beam}}$ ($A$ GeV) | $\sqrt{s_{NN}}$ (GeV) | $y_{\mathrm{beam}}$ | Year | Centrality | $\langle N_w \rangle$ | $N_{\mathrm{events}}$ | Momentum range (GeV) |
|---|---|---|---|---|---|---|---|
| 20 | 6.3 | 1.88 | 2002 | 7.2% | $349 \pm 1 \pm 5$ | 352 309 | 2.0–23.0 |
| 30 | 7.6 | 2.08 | 2002 | 7.2% | $349 \pm 1 \pm 5$ | 368 662 | 2.0–27.0 |
| 40 | 8.8 | 2.22 | 1999 | 7.2% | $349 \pm 1 \pm 5$ | 586 768 | 2.0–27.0 |
| 80 | 12.3 | 2.57 | 2000 | 7.2% | $349 \pm 1 \pm 5$ | 300 992 | 2.0–32.0 |
| 158 | 17.3 | 2.91 | 1996 | 5.0% | $362 \pm 1 \pm 5$ | 345 543 | 3.5–35.0 |

to 158$A$ GeV. Together with the data obtained at the AGS and the RHIC, our findings enable the study of energy dependence of $\phi$ production over a large range of collision energies.

## II. EXPERIMENT

The NA49 experiment at CERN is based on a fixed-target hadron spectrometer using heavy-ion beams from the SPS accelerator. Its main components are four large-volume time projection chambers for charged-particle tracking, two of which operate inside the magnetic field of two superconducting magnets, thus providing an excellent momentum measurement. Two larger main time projection chambers (MTPCs) are placed downstream, outside of the field, and enable particle identification by the measurement of the specific energy loss in the detector gas. The particle identification capabilities are enhanced by a time-of-flight (TOF) scintillator system behind the MTPCs, albeit in a restricted geometrical acceptance.

A thin lead foil with 1% interaction probability for Pb nuclei was used as a target. For the different runs, the magnetic field was scaled proportionally to the beam energies in order to have similar acceptance in the c.m. system.

The centrality of the reactions was determined from the energy deposited by the beam spectators in the zero-degree calorimeter, placed 20 m downstream of the target. By setting an upper limit on this energy, the online central trigger selected the 7.2% most central collisions at 20$A$–80$A$ GeV and the 10% most central collisions at 158$A$ GeV. The latter data set was restricted to 5% centrality in the offline analysis. The corresponding mean numbers of wounded nucleons were obtained by Glauber model calculations (see Table I). Details of the experimental apparatus can be found in Ref. [31].

## III. DATA ANALYSIS

### A. Event and track selection

Offline quality criteria were applied to the events selected by the online centrality trigger to suppress nontarget interactions, pileup, and incorrectly reconstructed events. The cut variables include the position and $\chi^2$ of the reconstructed vertex and the track multiplicity. For the central data sets used in this analysis, however, the impact of these quality cuts is marginal; only about 1% of all events were rejected. Table I shows the event statistics used in the analysis for the five data sets.

The analysis was restricted to tracks reconstructed in the MTPCs which could be assigned to the primary vertex. A minimal track length of 2 m out of the maximal 4 m in the MTPCs was required to suppress ghost or split tracks and to ensure a good resolution in $dE/dx$. Detailed studies including reconstruction of simulated tracks embedded into real raw data events showed that for such a selection of tracks, losses due to track reconstruction and high track density are negligible.

### B. Selection of kaon candidates

NA49 observes the $\phi$ meson through its hadronic decay into charged kaons. To reduce the large contribution of pions and protons to the combinatorial background, kaon candidates were selected based on their specific energy loss $dE/dx$ in the MTPCs. The mean $dE/dx$ of pions, kaons, and (anti-)protons was determined from TOF-identified

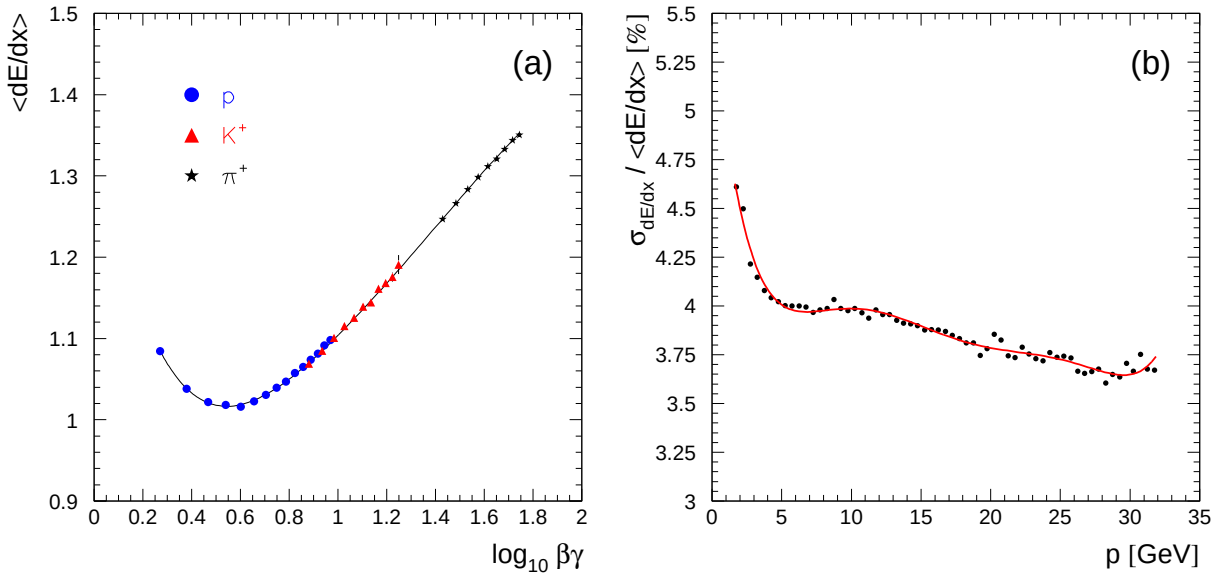


FIG. 1: (Color online) $dE/dx$ parametrization for the data set at 80$A$ GeV. (a) Mean $dE/dx$ as function of $\beta\gamma$ determined for TOF-identified pions, kaons, and protons; (b) $dE/dx$ resolution as function of momentum, obtained from the deconvolution of the energy loss spectra into the contributions of $\pi^+$, $K^+$, and $p$.

particles in the acceptance of the time-of-flight detectors and parametrized as a function of $\beta\gamma$ as shown in Fig. 1(a). This allowed one to extend the momentum range for the identification from the TOF acceptance to higher momenta. The lower momentum limit was given by either the MTPC acceptance or the crossing of the Bethe-Bloch curves of pions and kaons. The momentum limits for the different data sets are summarized in Table I.

Fixing the mean $dE/dx$ of kaons and protons to this parametrization, the resolution was obtained by unfolding the energy-loss spectra in momentum bins into the Gaussian contributions of the particle species ($p$, $K$, $\pi$, and $e$). The resolution is about 4% and has a slight momentum dependence which was again parametrized [Fig. 1(b)].

Kaon candidates were selected by a momentum-dependent $dE/dx$ window around the expectation value, the size of which was chosen to optimize the $\phi$ signal quality. In addition, the window had to be symmetric and large enough to minimize the sensitivity to the errors in the determination of the $dE/dx$ expectation value and resolution. A window of $\pm 1.5\,\sigma$ was found to be the best choice. This selection contains 87% of all kaons, giving an efficiency of 75% for the pair. The fraction of true kaons within the selected candidate track sample varies between 40% and 60%.

### C. Extraction of raw yields

The $\phi$ signal was obtained by calculating the invariant mass of all combinations of positive and negative kaon candidates in one event. To reconstruct the combinatorial background of uncorrelated pairs, candidates from different events were combined. The mixed-event spectrum was subtracted from the same-event spectrum after normalization to the same number of pairs [32]. Figure 2 shows the background-subtracted invariant-mass spectra in the total forward acceptance for different collision energies. In all cases, clear signals are observed at the expected position.

While the subtracted spectrum is flat on the right side of the signal, a depletion is observed between the peak and the threshold. As a possible source of this undershoot, the correlation of kaons stemming from different $\phi$ mesons has been discussed in Ref. [32]. In our case, it was shown by simulation that this effect is small thanks to the large acceptance of the NA49 MTPCs. Another possible source of the distortion is the reflection of other resonances, e.g., $\Delta^0 \rightarrow \pi^- p$, into the $K^+K^-$ spectrum by misidentification of pions and protons, as discussed in detail in Ref. [33]. This effect was shown to be present in our previous analysis of another data set [23], where the $dE/dx$ resolution was significantly worse. However, all such resonances would distort the spectrum over a broad range above threshold, which can be excluded by the observed flatness at higher masses. This conclusion is further strengthened by the observation that the depletion does not vanish when applying a stricter $dE/dx$ cut on the kaons. Hence, the undershoot is likely to originate from a true correlation of kaon pairs. Simulations show that it can be explained by final state strong interaction of kaons [34]. This is demonstrated in Fig. 3 by showing the $K^+K^-$ correlation

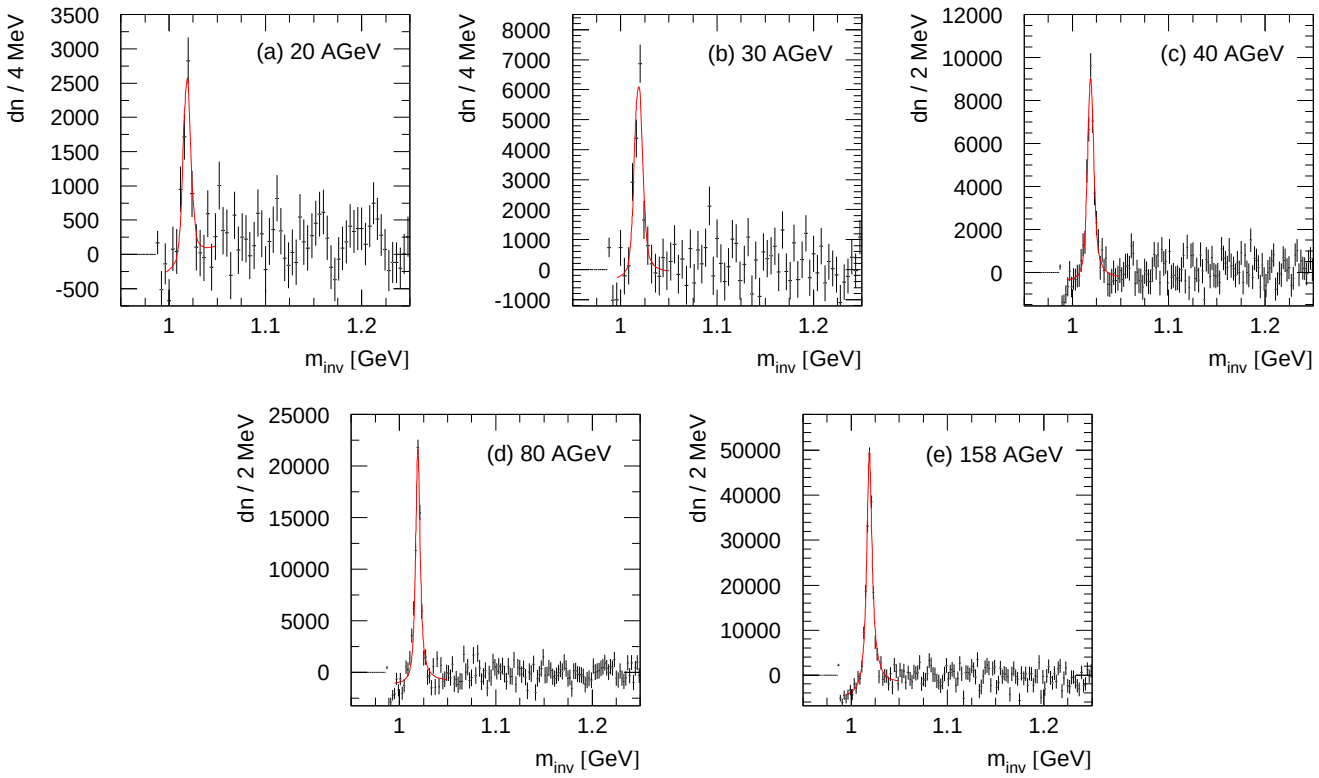


FIG. 2: (Color online) $K^+K^-$ invariant-mass spectra after subtraction of the combinatorial background in the forward rapidity hemisphere for the five different beam momenta. The full lines show the Breit-Wigner fits to the signals as described in the text. The bin size is 4 MeV for 20$A$ and 30$A$ GeV and 2 MeV for the other beam energies.

function in $q_{\rm inv} = \sqrt{(\vec{p}_1 - \vec{p}_2)^2 - (E_1 - E_2)^2}$ [Fig. 3(a)] and in $m_{\rm inv}$ [Fig. 3(b)]. While the repulsive interaction causes a depletion in $m_{\rm inv}$, the stronger attractive Coulomb effect is squeezed into 0.8 MeV above threshold and is thus hardly seen. In combination with the steeply rising unsubtracted $m_{\rm inv}$ distribution, this depletion can easily account for the deficit observed in the subtracted spectrum.

To correct this effect quantitatively by simulation is difficult and would moreover be model dependent. As the narrow signal is easily distinguished from the broad residual background, we accounted for the depletion by fitting a straight line in the vicinity of the peak. For the description of the signal itself, we used a relativistic $p$-wave Breit-Wigner distribution [35] of the form

$$\frac{dN}{dm} \propto \frac{m\Gamma(m)}{(m^2 - m_0^2)^2 + m_0^2\Gamma^2(m)} \tag{1}$$

with the mass-dependent width

$$\Gamma(m) = 2\,\Gamma_0 \left(\frac{q}{q_0}\right)^3 \frac{q_0^2}{q^2 + q_0^2}\,, \tag{2}$$

where $q := \sqrt{\frac{1}{4}m^2 - m_K^2}$ and $q_0 := \sqrt{\frac{1}{4}m_0^2 - m_K^2}$. This distribution was folded with a Gaussian representing the invariant-mass resolution $\sigma_m$ of the spectrometer. Since in general, mass resolution and width cannot be determined separately, we fixed the width to its book value $\Gamma_0 = 4.26\,$MeV [36], leaving $m_0$, $\sigma_m$, a normalization and two parameters for the linear background as free parameters for the fit, which was performed in the mass range 994–1050 MeV. It was checked by simulations that this procedure gives the correct values for position, width and integral of the distribution. As Fig. 2 demonstrates, the fit gives a good description of the signal. The numerical values of the fitted parameters are listed in Table II.

To obtain longitudinal and transverse spectra, the signal was extracted in rapidity and in $p_t$ bins, respectively, in the same way as in the total acceptance. Generally, the limited statistics prevented a simultaneous division into $y$-$p_t$

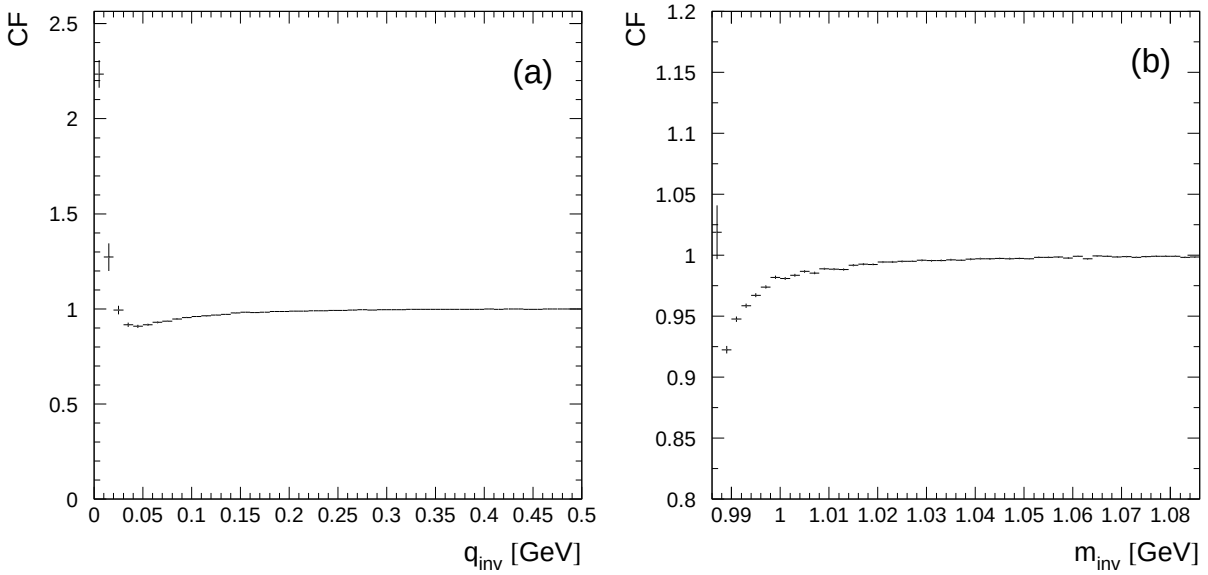


FIG. 3: $K^+K^-$ correlation function close to threshold in (a) $q_{\rm inv}$ and (b) $m_{\rm inv}$ [34].

bins. Thus, transverse momentum spectra could only be derived averaged over rapidity. To reduce the number of free fit parameters, $m_0$ and $\sigma_m$ were fixed for the fits in the phase space bins to the values obtained from the signal in the total acceptance. For the 158$A$ GeV data set, where the statistics in the signal allowed to do so, we checked that leaving these parameters free did not significantly alter the results. In particular, no significant dependence of $m_0$ or $\sigma_m$ on rapidity or $p_t$ was observed.

Since the straight-line background is only an approximation for the residual background in the vicinity of the signal, the stability of the fit against the variation of the fit region was checked. The parameters $m_0$ and $\sigma_m$ show no significant dependence. The variation of the normalization constants, which determine the fit integral, is in all bins far below the statistical error returned by the fit procedure. We conclude that the latter properly takes into account the possible variations of the baseline.

The raw yields in the phase-space bins were obtained by integrating the fit function from threshold up to $m_0+30\Gamma_0 \approx 1.148$ MeV. This mass cutoff is somehow arbitrary; the corresponding integral varies by about 3% for cutoff values from $m_0 + 10\Gamma_0$ to infinity. We take this as a systematic uncertainty due to the mass cutoff. Using alternatively a (analytically integrable) nonrelativistic Lorentz distribution for the fit does not change the integral by more than 1%.

### D. Geometrical acceptance

The geometrical acceptance of the NA49 detector for the decay $\phi \to K^+K^-$ was obtained double-differentially in $y$ and $p_t$ (integrated over azimuth) by GEANT simulations of the $\phi$ decay including in-flight decay of the kaon daughters, assuming an azimuthally flat $\phi$ emission and isotropic decay. The resulting acceptance is shown in Fig. 4 for 20$A$ and 158$A$ GeV. While the upper momentum limit for the daughter candidates restricts the acceptance at forward rapidity for the top SPS energy, at lower beam energies there is lack of acceptance near midrapidity because of the lower momentum limit for the daughter tracks and the increased losses due to in-flight decay for low-momentum kaons.

As the acceptance is a function of $y$ and $p_t$, the proper correction factor for a given extended phase-space bin (integrated either over $y$ or $p_t$) as used in the analysis is the mean acceptance

$$\overline{a}_S = \frac{\int\limits_S dy dp_t\, a(y,p_t)\, f(y,p_t)}{\int\limits_S dy dp_t\, f(y,p_t)}\,, \tag{3}$$

where $S$ denotes the region in the $y, p_T$ plane, $a(y,pt)$ the acceptance probability averaged over the azimuthal angle, and $f(y,p_t)$ the differential $\phi$ meson yield. For the rapidity distributions, the differential yields have in addition to be extrapolated to the full $p_t$ range. The extrapolation factor, however, is small (<5%) due to the large $p_t$ range covered by the experiment.

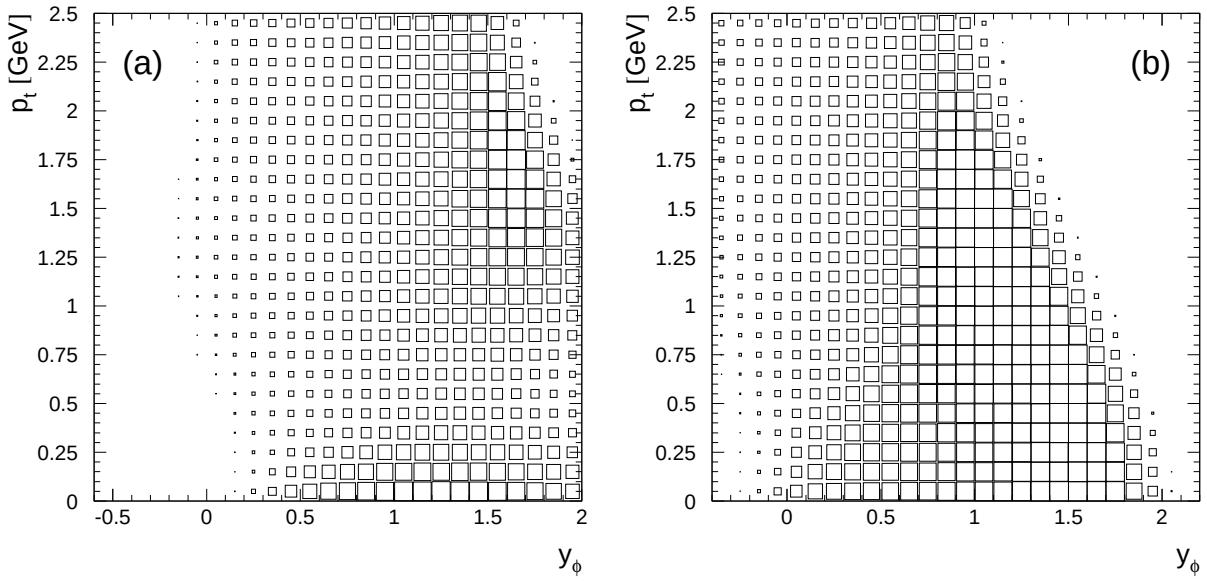


FIG. 4: Geometrical acceptance probability for $\phi \to K^+K^-$ including kaon decay in flight for (a) 20$A$ GeV and (b) 158$A$ GeV.

Both the acceptance correction and the extrapolation to full $p_t$ require the knowledge of the $y$ and $p_t$ dependence of $\phi$ meson yields, which leads to an iterative procedure (see Sec. III E).

### E. Spectra and yields

Apart from the differential acceptance correction, the raw yields obtained from the fit to the invariant-mass spectra were corrected for the branching ratio $\phi \to K^+K^-$ (49.1%) and the efficiency of kaon $dE/dx$ selection (75% for the pair), and normalized to the number of collisions. These global correction factors are common for all bins in phase space and for all beam energies.

The transverse spectra are fitted by the thermal ansatz

$$\frac{dn}{dp_t} \propto p_t \, e^{-m_t/T} \,, \tag{4}$$

where the transverse mass $m_t = \sqrt{m_0^2 + p_t^2}$. The distributions in rapidity were parametrized by a single Gaussian

$$\frac{dn}{dy} \propto e^{-\frac{y^2}{2\sigma_y^2}} \,. \tag{5}$$

As the parameters $T$ and $\sigma_y$ must be obtained by the analysis itself, an iterative procedure was employed. Starting from some reasonable parameter values, the acceptance correction was calculated according to Eq. (3), assuming factorization of the emission function $f(y, p_t)$ into the transverse and longitudinal distributions (4) and (5), i.e., independence of $T$ on rapidity. The corrected yields in the $p_t$ and $y$ bins were then fitted with the distributions (4) and (5), respectively, obtaining new values for $T$ and $\sigma_y$ which serve as input for the next iteration. Convergence of the method was reached after three to five steps. It was checked that the final results do not depend on the choice of start values for the parameters.

After the final step of the iteration, the yields in full phase space were obtained by summing up the measured yields in the rapidity distributions and numerically extrapolating Eq. (5) to the full rapidity range. In a similar way, the quantities $\langle p_t \rangle$, $\langle m_t \rangle$, and $\sigma_y$ were determined. The midrapidity yield $dn/dy$ was obtained directly from the fit function.

As demonstrated later in Fig. 7, the Gaussian parametrization gives a satisfactory description of the rapidity distribution for all data sets. However, because of the lack of midrapidity data points at the lower beam energies, an ambiguity for the extrapolation to full phase space arises. To check the sensitivity of the results to the assumed shape

of the rapidity distribution, we alternatively parametrized the latter by the sum of two Gaussian functions displaced symmetrically around midrapidity by a shift $a$:

$$\frac{dn}{dy} \propto e^{-\frac{(y-a)^2}{2\sigma_y^2}} + e^{-\frac{(y+a)^2}{2\sigma_y^2}} . \tag{6}$$

The width of this distribution will be characterized by its rms value. Total yield $\langle\phi\rangle$, midrapidity yield $dn_\phi/dy$ and $\mathrm{rms}_y$ were calculated for both parametrizations (5) and (6). The final values listed in Tables V and VI were calculated as the mean of the results of the two methods; their differences enter the systematic errors.

### F. Statistical and systematic errors

Statistical errors in the raw differential $\phi$ meson yields originate from the statistical bin-by-bin errors in the same-event and mixed-event invariant mass spectra, which were found to be in good approximation Poissonian and uncorrelated between mass bins. Then, the statistical errors in the event-mix subtracted invariant-mass spectrum was calculated as [32]

$$\sigma_i^2 = n_{0,i} + k^2 n_{\mathrm{em},i} , \tag{7}$$

where $n_{0,i}$ is the number of entries in mass bin $i$ in the same-event spectrum, $n_{\mathrm{em},i}$ the same number in the mixed-event spectrum, and $k$ the normalization constant for the event mix. These errors were propagated toward the raw differential yields by the least-squares fit of the Breit-Wigner distribution to the signal peak.

The acceptance calculation was performed with sufficiently high statistics such that the relative statistical error of the differential acceptance is below 1% and thus far below the uncertainty in the raw yields over the entire $y$, $p_t$ region used for the analysis. Finally, the errors in the acceptance-corrected differential yields are propagated through the least-square fits to the spectra to obtain the statistical uncertainties in the spectral parameters and the integrated quantities.

Systematic uncertainties in the uncorrected yields arise from the approximation of the residual background in the invariant-mass spectra as a straight line. This approximation is only valid in a limited mass range around the signal peak. Thus, the stability of the results of the Breit-Wigner fit against the variation of the fit range was checked. We found no significant dependence of the parameters $m_0$ and $\sigma_m$; the variation of the normalization constant, determining the fit integral, was in all $y$ and $p_t$ bins found to be smaller than the statistical error.

Another source of systematic error arises from the $dE/dx$ selection of kaon candidates. Uncertainties in the parametrization of the mean kaon $dE/dx$ and the resolution result in systematic deviations of the efficiency correction from its true value. To estimate this error, the analysis was repeated for different widths of the $dE/dx$ selection window around the kaon expectation value, applying the respective efficiency correction. This error was found to be the dominating one; for most raw yields, it is comparable to or slightly larger than the statistical one.

Imperfect detector description in the simulation leads to systematic uncertainties in the acceptance correction. To reduce possible errors, the analysis was restricted to phase-space regions where the acceptance is above 1%. The remaining error was estimated by repeating the analysis with varying acceptance conditions (minimal track length in the MTPCs). It was in all cases found to be much smaller than the error originating from the kaon selection by $dE/dx$.

As the spectral parameters enter the acceptance correction through Eq. (3), their uncertainties add to the systematic errors of the corrected yields. This was accounted for by determining the range of acceptance values allowed by the errors in $T$ and $\sigma_y$. In addition, for the rapidity bins close to beam rapidity, a possible deviation of the slope parameter by 50 MeV from its averaged value was taken into account in the acceptance correction. The resulting error, however, is small thanks to the large and approximately uniform $p_t$ acceptance.

The systematic errors in the corrected differential yields were assumed to be independent and added in quadrature. They were propagated to the respective errors in the spectral parameters by repeating the fit of Eqs. (4)–(6) with statistical and systematic errors added and comparing the resulting errors to those obtained from the fit with statistical errors only.

For the determination of the averaged quantities $\langle\phi\rangle$, $\langle p_r\rangle$, $\langle m_t\rangle$, and $\mathrm{rms}_y$, the summation of the measured differential yields as well as extrapolation to full phase space are required. The systematic errors of these observables were determined from the errors of the differential yields and the uncertainties in the spectral shapes.

TABLE II: Approximate number of detected $\phi$ mesons $S$, background-to-signal ratio $B/S$, signal-to-noise ratio SNR, position of the signal peak $m_0$, and invariant-mass resolution $\sigma_m$. The latter two were obtained by a Breit-Wigner fit to the signal peak (see text). The width was fixed to its literature value 4.26 MeV. $S$ and $B$ were calculated in a window of $\pm$ 4 MeV around the peak. The quoted errors are statistical only.

| $p_{\mathrm{beam}}$ ($A$ GeV) | $S$ | $B/S$ | SNR | $m_0$ (MeV) | $\sigma_m$ (MeV) |
|---|---|---|---|---|---|
| 20 | 6 500 | 70 | 9.4 | $1018.8 \pm 0.6$ | $2.6 \pm 0.9$ |
| 30 | 16 500 | 104 | 12.5 | $1018.4 \pm 0.5$ | $2.5 \pm 1.3$ |
| 40 | 37 000 | 53 | 26.2 | $1018.9 \pm 0.2$ | $2.1 \pm 0.3$ |
| 80 | 55 000 | 30 | 42.5 | $1019.1 \pm 0.1$ | $1.1 \pm 0.1$ |
| 158 | 180 000 | 72 | 49.4 | $1019.0 \pm 0.1$ | $1.8 \pm 0.1$ |

## IV. RESULTS

### A. Line shape

Table II summarizes the parameters obtained from the invariant-mass signals in the total acceptance. The signal quality decreases when going to lower beam energy because of both the reduced $\phi$ meson yield and the reduced acceptance due to the increased in-flight decay probability for the daughter kaons. At all five energies, the fitted peak position is slightly below the literature value of 1019.43 MeV [36]. We investigated the effect of an error in the normalization of the magnetic field used for momentum determination in the reconstruction chain and found that a bias of 1% in the magnetic field is needed to explain the observed shift. This is slightly above the momentum scale uncertainty deduced from a precision study of the $K^0_s$ signal. We thus cannot exclude that the deviation of the peak position is due to experimental effects.

The widths of the mass peaks obtained from the fits are consistent with those obtained from a full detector simulation and reconstruction. Their slight increase toward lower beam energies can be understood as the increasing influence of multiple scattering on lower momentum tracks. For the signal at 158$A$ GeV, we fitted simultaneously width and mass resolution and obtained $\Gamma_0 = (4.41 \pm 0.61)\,\mathrm{MeV}$, $\sigma_m = (1.81 \pm 0.26)\,\mathrm{MeV}$, i.e., no deviation from the free-particle width. Thus, within experimental uncertainties, we do not observe indications for a mass shift or a broadening of the $\phi$ meson.

The observation that the mass and width of the $\phi$ meson agree with the Particle Data Group values is in line with the results of AGS and RHIC experiments [27, 28, 29, 30]. It should be noted that because of the long lifetime of the $\phi$ meson ($\tau = 46$ fm), only a fraction decays inside the fireball. Thus, only a part of the $\phi$ mesons can be expected to be influenced by the surrounding medium.

### B. Transverse momentum spectra

The transverse momentum spectra obtained for the five beam energies are shown in Fig. 5; numerical data are given in Table III. In all cases, the thermal distribution (4) gives a good description of the data; the fit parameters are summarized in Table IV. At top SPS energy with the best signal quality, a modest deviation from the fit function is indicated by the $\chi^2$/ndf of 1.5. A slight curvature of the transverse mass spectrum at this energy, as expected from a hydrodynamical expansion scenario, is visible for this energy in Fig. 6(a). For the other energies, no deviations from pure exponential behavior can be seen within the experimental uncertainties.

The transverse momentum spectrum can be also characterized by its first moment or the average transverse mass. These parameters were calculated from the measured data points and extrapolated to full $p_t$ using the exponential fit function. As the extrapolation contributes only marginally because of the large $p_t$ coverage, $\langle p_t \rangle$ and $\langle m_t \rangle - m_0$ are largely independent of the spectral shape. Their values are also listed in Table IV.

The assumption of the slope parameter being independent of $y$ could be checked for 158$A$ GeV, where statistics allowed us to extract transverse spectra in four different rapidity bins. The resulting slope parameters are shown in Fig. 6(b). Within the measured rapidity range, we observe no significant change of the slope parameter with $y$. Using the $y$-dependent slope parameters for correcting the rapidity distribution had no sizable effect on the results.

The spectrum obtained for 158$A$ GeV agrees with that from an earlier publication [23] of the NA49 experiment, which was based on the analysis of an older data set at the same beam energy. For comparison, the previously

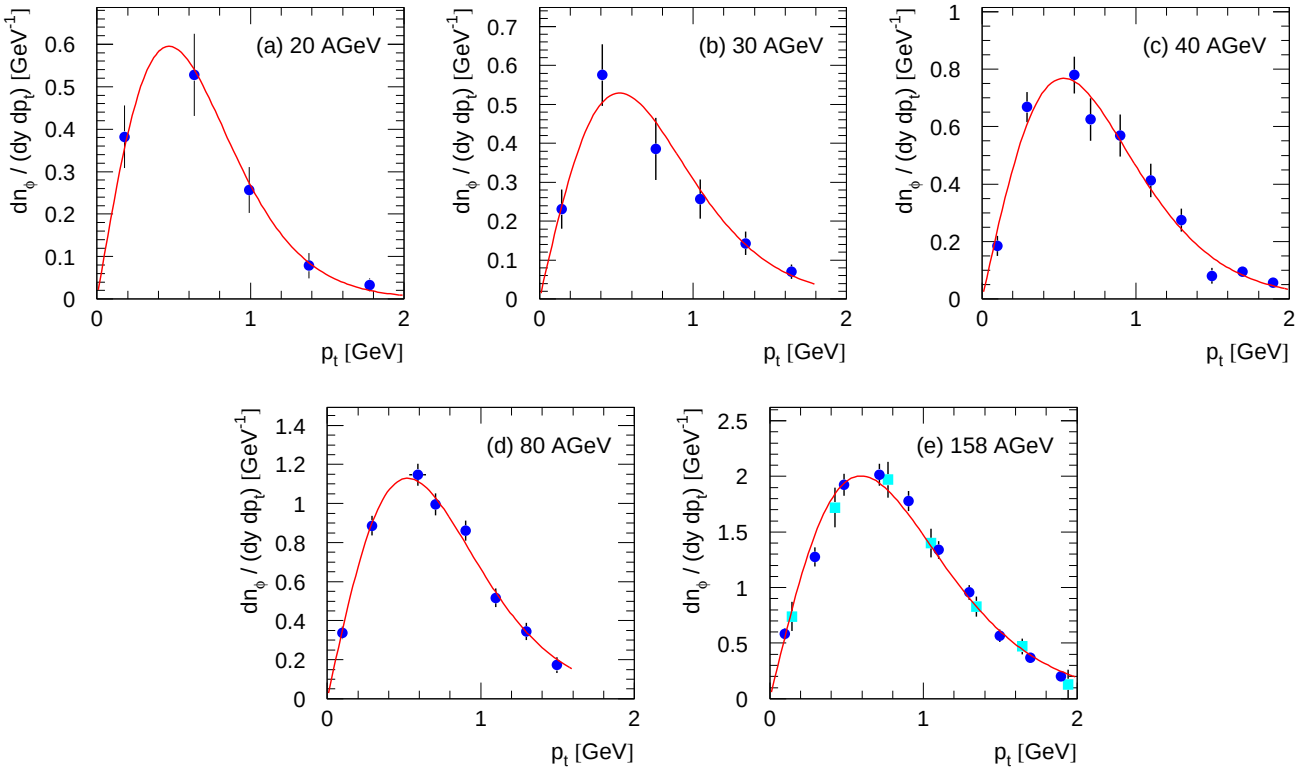


FIG. 5: (Color online) $\phi$ transverse momentum spectra integrated over the rapidity intervals given in Table IV. The full lines show the fits of thermal distributions (4). The squared symbols denote previously published results [23]. Only statistical errors are shown.

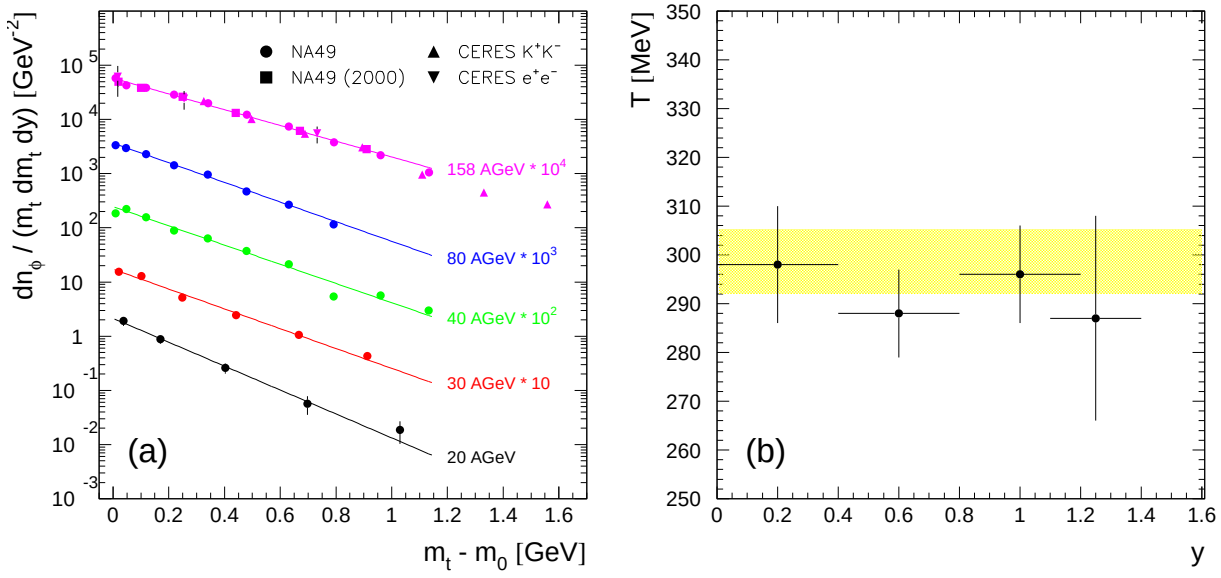


FIG. 6: (Color online) (a) $\phi$ transverse mass spectra integrated over the rapidity intervals given in Table IV. The exponential fits indicated by the full lines correspond to the fits shown in Fig. 5. The spectra for different beam energies are scaled for better visibility. Only statistical errors are shown. The data at 158$A$ GeV are compared with previously published results of NA49 [23] and CERES [25]. (b) Slope parameter as function of rapidity at 158$A$ GeV. The values agree within errors with that obtained from the $y$-integrated $p_t$ spectrum, the latter indicated with its standard deviation by the shaded bar.

TABLE III: Differential $\phi$ meson yields in the $p_t$ (left) and $y$ (right) distributions. Data in the $p_t$ bins are integrated over the rapidity ranges given in Table IV. The errors are statistical.

| $p_t$ (GeV) | $dn/(dydp_t)$ (GeV$^{-1}$) | y | $dn/dy$ |
|---|---|---|---|
| | $E_{beam} = 20A$ GeV | | |
| 0.0–0.4 | $0.382 \pm 0.074$ | 0.2–0.6 | $1.043 \pm 0.250$ |
| 0.4–0.8 | $0.528 \pm 0.097$ | 0.6–1.0 | $0.536 \pm 0.077$ |
| 0.8–1.2 | $0.257 \pm 0.054$ | 1.0–1.4 | $0.159 \pm 0.033$ |
| 1.2–1.6 | $0.079 \pm 0.030$ | 1.4–1.8 | $0.032 \pm 0.017$ |
| 1.6–2.0 | $0.033 \pm 0.015$ | | |
| | $E_{beam} = 30A$ GeV | | |
| 0.0–0.3 | $0.231 \pm 0.051$ | 0.3–0.6 | $0.735 \pm 0.194$ |
| 0.3–0.6 | $0.578 \pm 0.079$ | 0.6–0.9 | $0.651 \pm 0.090$ |
| 0.9–1.2 | $0.386 \pm 0.079$ | 0.9–1.2 | $0.456 \pm 0.052$ |
| 1.2–1.5 | $0.257 \pm 0.050$ | 1.2–1.5 | $0.193 \pm 0.036$ |
| 1.5–1.8 | $0.070 \pm 0.019$ | 1.5–1.8 | $0.097 \pm 0.029$ |
| | $E_{beam} = 40A$ GeV | | |
| 0.0–0.2 | $0.185 \pm 0.035$ | 0.3–0.6 | $1.067 \pm 0.108$ |
| 0.2–0.4 | $0.668 \pm 0.052$ | 0.6–0.9 | $0.756 \pm 0.059$ |
| 0.4–0.6 | $0.780 \pm 0.064$ | 0.9–1.2 | $0.611 \pm 0.038$ |
| 0.6–0.8 | $0.625 \pm 0.075$ | 1.2–1.5 | $0.348 \pm 0.028$ |
| 0.8–1.0 | $0.569 \pm 0.073$ | 1.5–1.8 | $0.188 \pm 0.023$ |
| 1.0–1.2 | $0.413 \pm 0.059$ | | |
| 1.2–1.4 | $0.275 \pm 0.040$ | | |
| 1.4–1.6 | $0.081 \pm 0.028$ | | |
| 1.6–1.8 | $0.086 \pm 0.019$ | | |
| 1.8–2.0 | $0.057 \pm 0.014$ | | |
| | $E_{beam} = 80A$ GeV | | |
| 0.0–0.2 | $0.337 \pm 0.031$ | -0.3–0.0 | $1.591 \pm 0.304$ |
| 0.2–0.4 | $0.886 \pm 0.051$ | 0.0–0.3 | $1.474 \pm 0.138$ |
| 0.4–0.6 | $1.148 \pm 0.057$ | 0.3–0.6 | $1.258 \pm 0.086$ |
| 0.6–0.8 | $0.996 \pm 0.056$ | 0.6–0.9 | $1.351 \pm 0.062$ |
| 0.8–1.0 | $0.861 \pm 0.052$ | 0.9–1.2 | $1.041 \pm 0.049$ |
| 1.0–1.2 | $0.517 \pm 0.048$ | 1.2–1.5 | $0.718 \pm 0.043$ |
| 1.2–1.4 | $0.344 \pm 0.045$ | 1.5–1.8 | $0.408 \pm 0.037$ |
| 1.4–1.6 | $0.173 \pm 0.040$ | 1.8–2.1 | $0.197 \pm 0.040$ |
| | $E_{beam} = 158A$ GeV | | |
| 0.0–0.2 | $0.582 \pm 0.053$ | 0.0–0.2 | $2.557 \pm 0.166$ |
| 0.2–0.4 | $1.275 \pm 0.086$ | 0.2–0.4 | $2.386 \pm 0.121$ |
| 0.4–0.6 | $1.924 \pm 0.098$ | 0.4–0.6 | $2.229 \pm 0.098$ |
| 0.6–0.8 | $2.016 \pm 0.099$ | 0.6–0.8 | $2.202 \pm 0.089$ |
| 0.8–1.0 | $1.778 \pm 0.092$ | 0.8–1.0 | $1.974 \pm 0.090$ |
| 1.0–1.2 | $1.339 \pm 0.080$ | 1.0–1.2 | $1.816 \pm 0.094$ |
| 1.2–1.4 | $0.956 \pm 0.067$ | 1.2–1.4 | $1.636 \pm 0.105$ |
| 1.4–1.6 | $0.567 \pm 0.055$ | 1.4–1.6 | $1.528 \pm 0.126$ |
| 1.6–1.8 | $0.370 \pm 0.044$ | 1.6–1.8 | $1.125 \pm 0.171$ |
| 1.8–2.0 | $0.200 \pm 0.034$ | | |

published data are shown by the square symbols in Figs. 5(e) and 6(a). There is agreement with the results of the CERES experiment in both decay channels $\phi \to K^+K^-$ and $\phi \to e^+e^-$ [25], as also demonstrated in Fig. 6(a). The data disagree with the spectrum measured by the NA50 experiment in the di-muon decay channel $\phi \to \mu^+\mu^-$, where a significantly smaller slope was obtained [24].

TABLE IV: Rapidity range (in c.m. system), $p_t$ range, slope parameter $T$, $\chi^2$ per degree of freedom, average $p_t$, and average $m_t$ for the transverse momentum spectra. $T$ and $\chi^2$ are results from the fit of Eq. (4) to the spectrum; $\langle p_t \rangle$ and $\langle m_t \rangle - m_0$ were obtained by summation over the data points and extrapolation to full $p_t$ using the fit function. The first error is statistical, the second one systematic.

| $p_{\rm beam}$ ($A$ GeV) | $y$ range | $p_t$ range (GeV) | $T$ (MeV) | $\chi^2$/ndf | $\langle p_t \rangle$ (MeV) | $\langle m_t \rangle - m_0$ [MeV] |
|---|---|---|---|---|---|---|
| 20 | 0.0–1.8 | 0.0–2.0 | $196.8 \pm 19.5 \pm 20.2$ | 1.06/3 | $650.9 \pm 34.2 \pm 40.2$ | $229.5 \pm 20.1 \pm 23.6$ |
| 30 | 0.0–1.8 | 0.0–1.8 | $237.4 \pm 17.8 \pm 22.9$ | 2.03/4 | $738.9 \pm 28.3 \pm 46.3$ | $284.6 \pm 17.3 \pm 28.4$ |
| 40 | 0.0–1.5 | 0.0–2.0 | $244.6 \pm 9.0 \pm 5.8$ | 12.42/8 | $763.4 \pm 15.8 \pm 14.3$ | $297.8 \pm 10.0 \pm 9.2$ |
| 80 | 0.0–1.7 | 0.0–1.6 | $239.8 \pm 8.3 \pm 10.9$ | 3.48/6 | $756.4 \pm 11.5 \pm 22.5$ | $292.6 \pm 7.6 \pm 15.3$ |
| 158 | 0.0–1.0 | 0.0–2.0 | $298.7 \pm 6.6 \pm 10.6$ | 12.06/8 | $883.5 \pm 9.9 \pm 21.3$ | $378.3 \pm 6.7 \pm 15.2$ |

TABLE V: Parameters of the single-Gauss fit (5) and the double-Gauss fit (6) to the rapidity distributions. The RMS was calculated from the data points and extrapolated to the full rapidity range using the average of the two parametrizations. The first error is statistical, the second one systematic.

| $p_{\rm beam}$ ($A$ GeV) | $\sigma_1$ | $\chi^2_1$/ndf | $\sigma_2$ | $a$ | $\chi^2_2$/ndf | ${\rm rms}_y$ |
|---|---|---|---|---|---|---|
| 20 | $0.572 \pm 0.037 \pm 0.030$ | 0.042/2 | $0.425 \pm 0.026 \pm 0.022$ | 0.425 | 0.75/2 | $0.582 \pm 0.031 \pm 0.040$ |
| 30 | $0.752 \pm 0.047 \pm 0.057$ | 2.02/3 | $0.538 \pm 0.028 \pm 0.032$ | 0.538 | 1.03/3 | $0.769 \pm 0.030 \pm 0.062$ |
| 40 | $0.863 \pm 0.033 \pm 0.042$ | 3.14/4 | $0.696 \pm 0.118 \pm 0.036$ | $0.487 \pm 0.149 \pm 0.051$ | 3.10/3 | $0.852 \pm 0.015 \pm 0.038$ |
| 80 | $1.016 \pm 0.028 \pm 0.033$ | 17.55/6 | $0.658 \pm 0.035 \pm 0.043$ | $0.682 \pm 0.029 \pm 0.043$ | 4.12/5 | $0.974 \pm 0.024 \pm 0.074$ |
| 158 | $1.451 \pm 0.086 \pm 0.012$ | 2.36/7 | | | | $1.444 \pm 0.021 \pm 0.054$ |

### C. Rapidity distributions and yields

Figure 7 shows the rapidity distributions, which for all five energies are in good agreement with both the single-Gaussian and the double-Gaussian parametrization (see curves). Numerical data are given in Table III. For the data sets at 20$A$ and 30$A$ GeV, due to the low number of data points, the double-Gaussian fit was constrained to $a = \sigma_y$ as suggested by the data at 40$A$ and 80$A$ GeV.

Only at 80$A$ GeV is the complete forward hemisphere covered. At 158$A$ GeV, large rapidities are not measured because of the upper momentum cut on the secondary kaons. Since kaons below 2 GeV laboratory momentum cannot be reliably identified by $dE/dx$ because of the crossing of the Bethe-Bloch curves, no signal could be extracted at midrapidity for the lower three beam energies. The uncertainties in the extrapolation toward midrapidity is demonstrated by the difference of the two parametrizations. It adds to the systematic error of the total yield and, in particular, to that of $dn/dy$ at midrapidity. Table V lists the parameters obtained by the two fit functions, respectively.

Alternatively, the rapidity distributions can be characterized by their second moments in a model-independent fashion. The root mean square of the distributions was calculated from the measured data and extrapolated to the full rapidity range using the parametrizations (5) and (6). The average of the two results is listed in Table V.

Total yields were obtained by summation of the data points in the rapidity spectra and extrapolation to the full rapidity range by the average of the fit functions. The midrapidity yield $dn/dy$ was calculated analytically from the average of the fit functions. For the determination of statistical and systematic errors, the correlation of the spectral parameters were properly taken into account. The results for the mean multiplicity of $\phi$ mesons $\langle \phi \rangle$ and for the midrapidity yield $dn_\phi/dy$ are listed in Table VI.

All results obtained at 158$A$ GeV are consistent within statistical errors with NA49 results published earlier [23], which were obtained from a data set taken in 1995 (squared symbols in Fig. 7(e). The main difference of the two data sets is an improved $dE/dx$ resolution, resulting in a reduced pion contamination of the kaon candidate sample. The cleaner kaon identification reduces the distortions in the background-subtracted invariant-mass spectrum induced by resonances with a pion as decay daughter [33], thus leading to a smaller systematic error of the Breit-Wigner fit to the spectrum. We thus prefer to use the newly obtained results at 158$A$ GeV for the discussion.

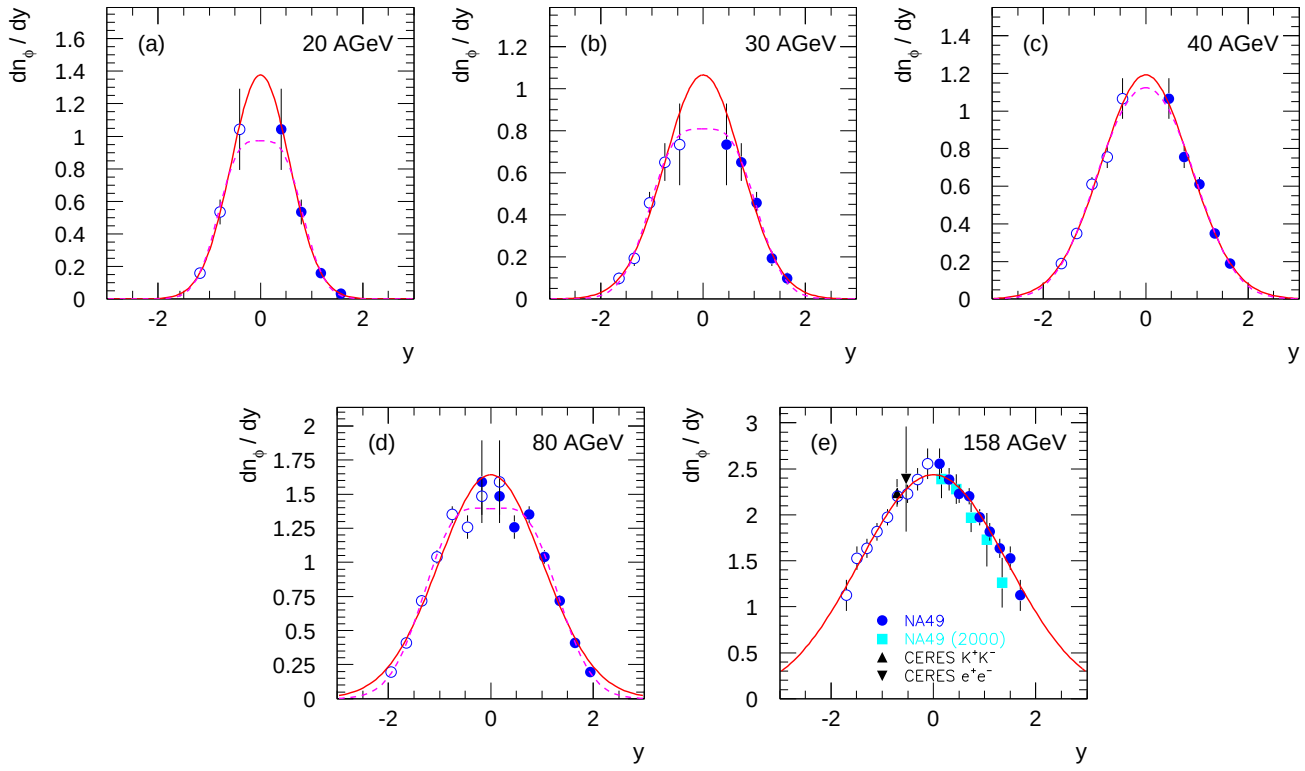


FIG. 7: (Color online) $\phi$ rapidity distributions. The solid points refer to measured data, the open points are reflected at midrapidity. The full lines show the parametrization by a single Gaussian (5), the dashed lines that by the sum of two Gaussians (6). The data at 158$A$ GeV are compared with previously published results of NA49 [23] and CERES [25]. Only statistical errors are shown.

TABLE VI: Total $\phi$ multiplicity $\langle\phi\rangle$ and midrapidity yield $dn_\phi/dy$ calculated from the rapidity distributions of Fig. 7. The first error is statistical, the second one systematic.

| $p_{\rm beam}$ ($A$ GeV) | $\langle\phi\rangle$ | $dn_\phi/dy(y_{\rm c.m.})$ |
|---|---|---|
| 20 | $1.89 \pm 0.31 \pm 0.22$ | $1.17 \pm 0.23 \pm 0.38$ |
| 30 | $1.84 \pm 0.22 \pm 0.29$ | $0.94 \pm 0.13 \pm 0.30$ |
| 40 | $2.55 \pm 0.17 \pm 0.19$ | $1.16 \pm 0.16 \pm 0.14$ |
| 80 | $4.04 \pm 0.19 \pm 0.31$ | $1.52 \pm 0.11 \pm 0.22$ |
| 158 | $8.46 \pm 0.38 \pm 0.33$ | $2.44 \pm 0.10 \pm 0.08$ |

## V. DISCUSSION

The enhancement of relative strangeness production in heavy-ion collisions with respect to proton-proton reactions is a well-known fact. In an earlier publication [23], the enhancement factor for the $\phi$ meson at top SPS energy was found to be $3.0 \pm 0.7$, thus larger than for kaons and $\Lambda$, but smaller than for multistrange hyperons. We calculate the $\phi$ enhancement by normalizing the measured $\phi$ meson yield in $A+A$ by the number of wounded nucleon pairs and dividing by the corresponding yield in $p+p$. For the lower beam energies, no reference measurements in elementary collisions are available. Here, we employ a parametrisation of the $\phi$ excitation function in $p+p$ collisions as described in Ref. [27]. For top SPS energy and RHIC, the $\phi$ meson yield measured in $p+p$ [23, 29] was used. Figure 8 shows the resulting enhancement factor

$$E_\phi := \frac{2\,\langle\phi\rangle_{A+A}}{N_w\,\langle\phi\rangle_{p+p}} \tag{8}$$

as a function of energy per nucleon pair. The measurement of the E917 Collaboration at AGS ($p_{\rm beam} = 11.7A$ GeV) was extrapolated to full phase space assuming the same rapidity distribution as for $K^-$ as suggested by the authors [27].

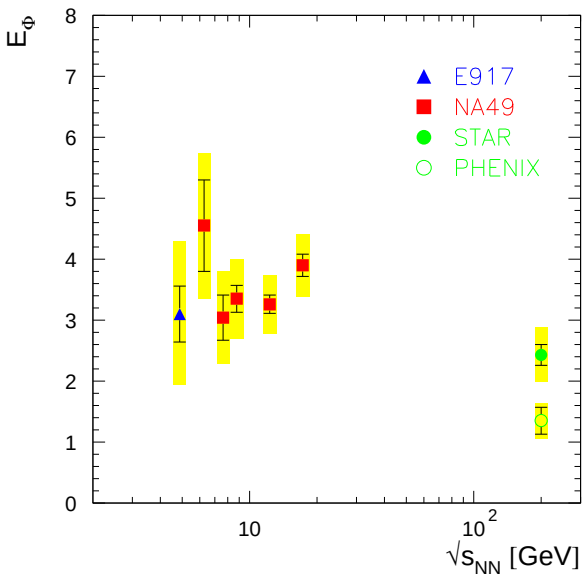


FIG. 8: (Color online) $\phi$ enhancement factor $E_\phi$ [see Eq. (8)] as function of energy per nucleon pair. Data from the AGS [27] and the SPS refer to multiplicities in full phase space, data from the RHIC [29, 30] to midrapidity yields. The shaded boxes represent the systematic errors.

In the AGS/SPS energy region, the value of $E_\phi$ lies between 3 and 4, and within our experimental uncertainties we find no systematic variation here. At RHIC energies, the enhancement appears to be lower, significantly so, should the PHENIX result be validated. It should be noted, however, that the RHIC values were derived from midrapidity data while at lower energies phase-space integrated yields were used.

In the context of statistical models, the enhancement of strangeness production can be interpreted as a result of the release of suppression due to strangeness conservation when going from small $(p+p)$ to large (central $A+A$) systems. Technically, this is reflected in the application of the canonical ensemble for small systems, while large systems can be described by the grand-canonical ensemble. In this picture, a smaller enhancement at RHIC energies points to the fact that at such high energies, strangeness is produced with sufficient abundance for the canonical suppression to be relaxed even in $p+p$ collisions. However, in a purely hadronic picture, canonical suppression does not act on the $\phi$ meson because it is a strangeness-neutral hadron. Enhanced $\phi$ production can thus be attributed either to enhanced strangeness production in a partonic stage of the collision or to the coalescence of kaons which suffer canonical suppression also in a hadronic scenario.

The hadrochemical models have been extended not only to fit hadron multiplicities for a given reaction but also to describe the energy dependence of particle yield ratios by a smooth variation of the relevant parameters $T$ and $\mu_B$ with collision energy [14, 37]. Here, the energy dependence of temperature and baryochemical potential is obtained by a parametrization of the values for $T$ and $\mu_B$ obtained from fits to particle yield ratios at various collision energies. The model reproduces many yield ratios of the bulk hadrons; however, this does not hold for the $\phi$ meson, as shown in Fig. 9(a), where the measured excitation function of the $\langle\phi\rangle/\langle\pi\rangle$ ratio $[\langle\pi\rangle = 1.5(\langle\pi^+\rangle + \langle\pi^-\rangle)]$ is compared with the model prediction. The relative $\phi$ meson yields at the SPS are overpredicted by factors of up to 2. The situation remains essentially unchanged when midrapidity ratios are considered instead of integrated yields [Fig. 9(b)]. At the RHIC, there is a large experimental ambiguity as a result of the different results on $\phi$ production obtained by the STAR and PHENIX experiments [29, 30].

A better description of the data is obtained if a strangeness saturation parameter $\gamma_s$ is allowed. The corresponding model predictions [8] for the $\phi$ multiplicity, resulting from a fit to the hadron abundances at 11.7$A$, 30$A$, 40$A$, 80$A$, and 158$A$ GeV, are compared with the data in Fig. 10 (solid points). Note that this model does not provide a continuous description of the energy dependence; the points are only connected to guide the eye. The agreement with the measurements at the higher SPS energies is very good. The successful application of the saturation parameter $\gamma_s$ on the strangeness-neutral $\phi$ meson for $p_{\rm beam} \geq 40A$ GeV again suggests that the strangeness content at chemical freeze-out is determined on a partonic level for these energies.

Final state interactions after chemical freeze-out could change the equilibrium $\phi$ yield and spectra. In particular, scattering of the daughter kaons with other produced hadrons would lead to a loss of the $\phi$ signal in the experimentally

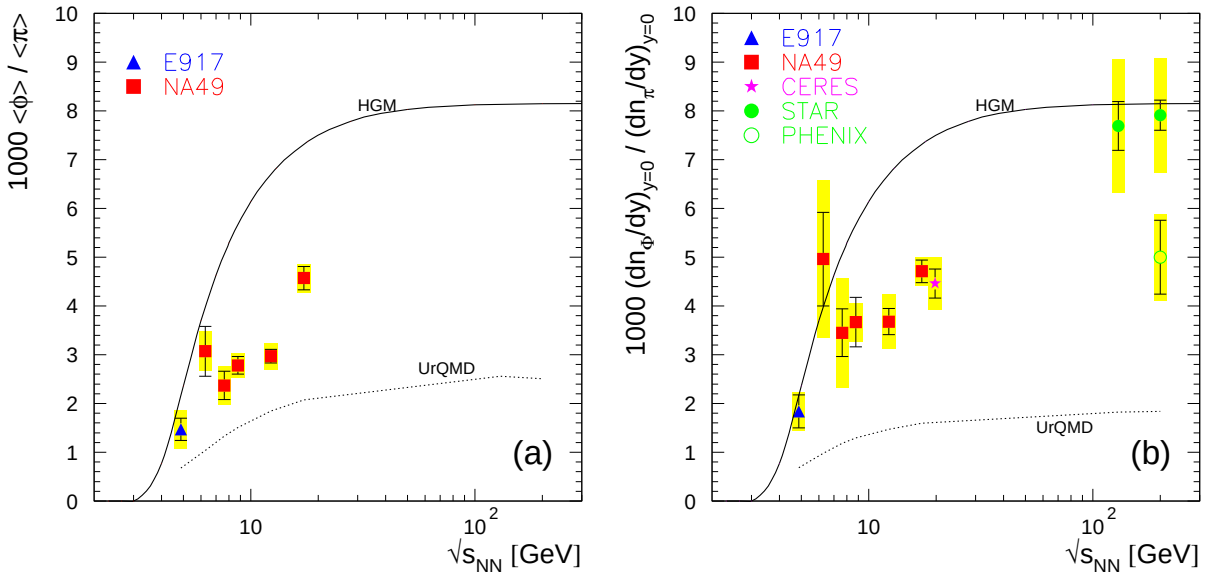


FIG. 9: (Color online) $\langle\phi\rangle/\langle\pi\rangle$ ratio (a) in full phase space and (b) at midrapidity as function of energy per nucleon pair [$\langle\pi\rangle = 1.5(\langle\pi^+\rangle+\langle\pi^-\rangle)$]. The CERES data point [25] was displaced horizontally for visibility. Note that the CERES measurement is at $y \approx y_{\rm c.m.} - 0.5$. The full line shows the predictions of the extended hadron gas model (HGM) with strangeness equilibration [37], the dashed curves those obtained with UrQMD 1.3 [17]. The shaded boxes represent the systematic errors.

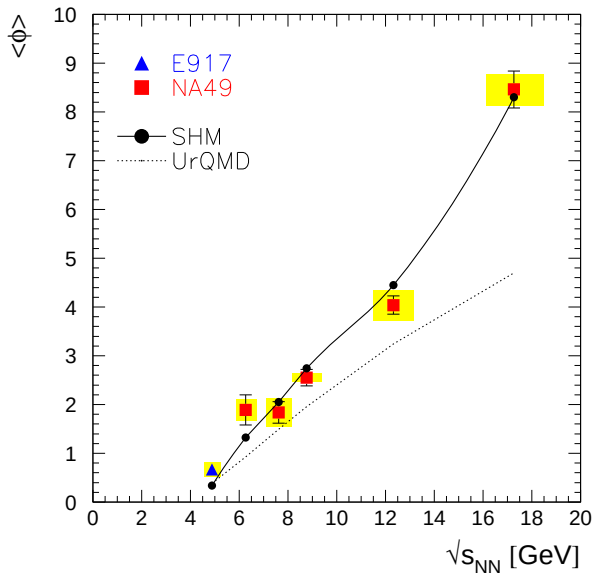


FIG. 10: (Color online) $\phi$ multiplicity in central $A+A$ collisions as function of energy per nucleon pair. The solid points denote the results of the statistical hadronization model (SHM) which allows a deviation from strangeness equilibrium [8]. They are connected by the solid line to guide the eye. The dotted curve shows the $\phi$ yield predicted by the UrQMD 1.3 model [17]. The shaded boxes represent the systematic errors.

observed decay channel, predominantly at small rapidities and low values of $p_t$. Such a loss is not expected in the leptonic decay modes, since electrons or muons will leave the fireball without interaction. A comparison of the measured $m_t$ spectrum via the $K^+K^-$ and $e^+e^-$ decay channels [see Fig. 6(a)] indicates that the effect cannot be large. To study the effect on the total yield, we used the string-hadronic transport model UrQMD [17]. It was found that only about 8% of the decayed $\phi$ mesons are lost for detection due to rescattering of their daughter particles, independent of collision energy. Similar results have been obtained with the RQMD model [19]. The effect is thus

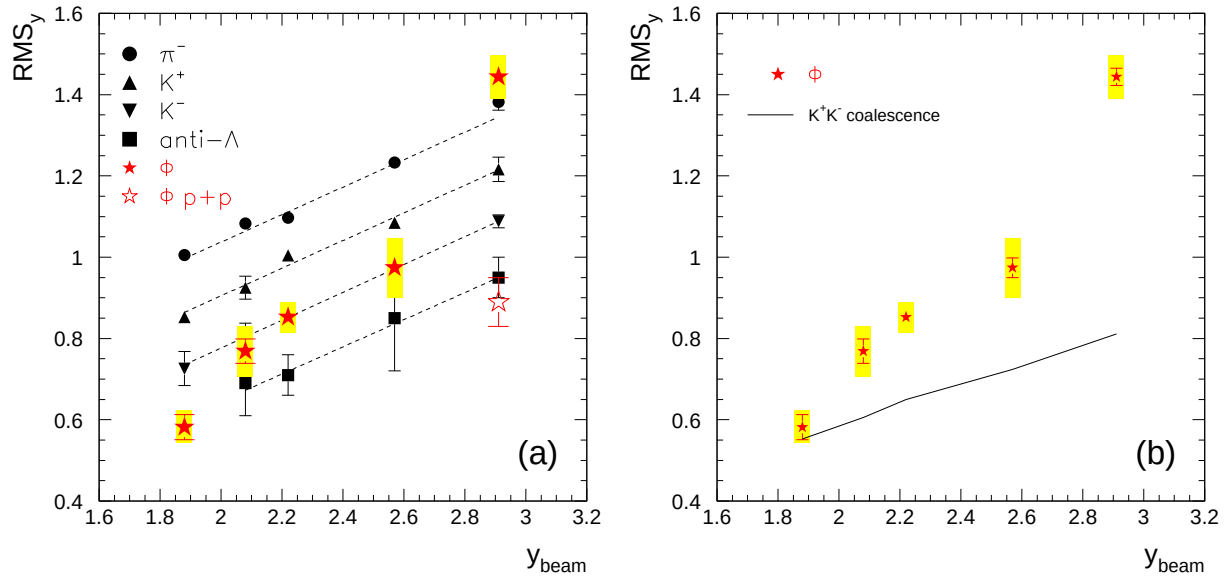


FIG. 11: (Color online) (a) Widths of the rapidity distributions of $\pi^-$, $K^+$, $K^-$, and $\phi$ in central Pb + Pb collisions at SPS energies as function of beam rapidity [38, 39]. The dashed lines are to guide the eye. The open star denotes the $\phi$ rapidity width measured in $p+p$ collisions [23]. (b) Widths of the $\phi$ rapidity distributions in central Pb+Pb collisions compared with the expectations in a kaon coalescence picture [Eq. (9)]. The shaded boxes represent the systematic errors (shown only for $\phi$ mesons).

not sufficient to account for the deviation of the relative $\phi$ multiplicities from their equilibrium values.

On the other hand, $\phi$ mesons can be produced by $KK$ scattering. In fact, kaon coalescence is the dominant ($\approx$ 70%) production mechanism for the $\phi$ in UrQMD, again for all investigated collision systems. As shown by the dotted curve in Fig. 10, the model gives a reasonable description of the $\phi$ meson yields at lower energies, whereas it starts to deviate from the measurements at intermediate SPS energies. The discrepancy with data is more pronounced when studying the $\langle\phi\rangle/\langle\pi\rangle$ ratio (Fig. 9) because UrQMD overestimates the pion yields at SPS energies by about 30%.

The hypothesis that the $\phi$ meson is produced predominantly by kaon coalescence can be tested by comparing the $\phi$ and kaon distributions in phase space. Figure 11(a) shows the width of the $\phi$ rapidity distribution as a function of beam rapidity at SPS energies, together with that measured for $\pi^-$, $K^+$, and $K^-$ [38, 39]. The $\phi$ meson width does not fit into the systematics observed for the other particle species but increases much faster with energy. While at 20$A$ GeV, the $\phi$ rapidity distribution is narrower than that of $K^-$, we find it at top SPS energy comparable to the pions. In addition, at 158$A$ GeV it is much larger in central Pb + Pb collisions than measured in $p+p$ collisions at the same energy [23], a feature which is not observed for other particle species.

In the kaon coalescence picture, there would be a tendency for the $\phi$ rapidity distribution to be narrower than those of the kaons. In an ideal case, neglecting correlations,

$$\frac{1}{\sigma_\phi^2} = \frac{1}{\sigma_{K^+}^2} + \frac{1}{\sigma_{K^-}^2}\,, \tag{9}$$

where the distributions were approximated by Gaussians. As shown in Fig. 11(b), the $\phi$ data rule out kaon coalescence as dominant formation mechanism for beam energies above 30$A$ GeV. Only at 20$A$ GeV, the observed rapidity widths are consistent with the coalescence picture. As mentioned before, this would also explain the $\phi$ enhancement at low energies, where a transient deconfined state is not expected.

The observation that models based on a purely hadronic reaction scenario have serious problems in describing relative strangeness production in the upper SPS energy range is not unique to the $\phi$ meson but holds for kaons and other strange particles, too. It has been related to the onset of deconfinement at around 30$A$ GeV as predicted by the statistical model of the early stage [18]. A striking experimental evidence is the narrow maximum in the $K^+/\pi^+$ ratio at this energy [38, 39]. A similar structure is, within experimental errors, not observed for the $\phi$ meson (Fig. 9); instead, the energy dependence of the relative $\phi$ meson yield resembles that of the $K^-$. This can be understood since the $K^+$ yield is in good approximation proportional to the total strangeness production, which is not the case for $K^-$ and $\phi$ because a large, energy-dependent fraction of $s$ quarks is carried by hyperons.

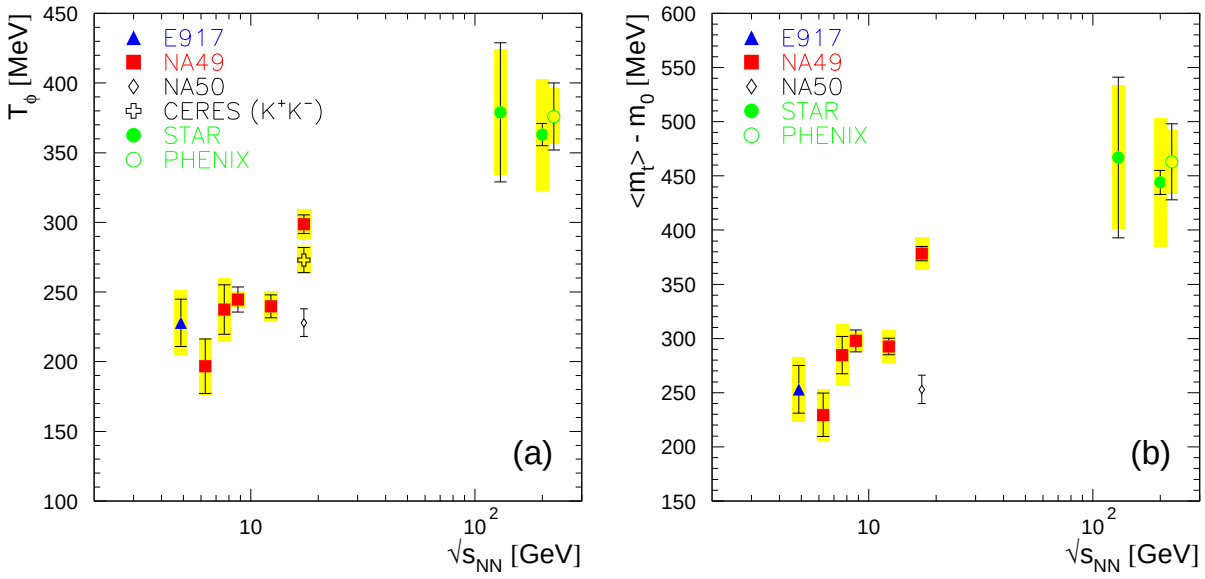


FIG. 12: (Color online) (a) Inverse slope parameter $T$ and (b) average transverse mass $\langle m_t \rangle - m_0$ of the $\phi$ meson in central $A + A$ collisions as function of energy per nucleon pair. The data from E917 [27] were averaged over the measured rapidity interval (see Table IV). Results from NA50 [24] and RHIC [28, 29, 30] were obtained at midrapidity, the result from CERES at $y = -0.71$. Data from NA49 are integrated over rapidity. The PHENIX data point was slightly displaced horizontally for visibility. For the NA49 data, $\langle m_t \rangle$ was calculated from the transverse momentum spectra using an exponential extrapolation to full $p_t$. For the other data sets, it was derived analytically from the exponential fit function. The shaded boxes represent the systematic errors.

The energy dependences of both the inverse slope parameter and the mean transverse mass of the $\phi$ meson are shown in Fig. 12. The transverse mass spectra of the $\phi$ are well described by exponential fits [see Fig. 6(a)]; consequently, the two parameters show a similar behavior. Over the energy range AGS–SPS–RHIC, there is an overall tendency for both parameters to increase. However, a constancy of the values in the lower SPS energy range, as has been observed for pions, kaons, and protons [39]—a fact interpreted as being consistent with a mixed partonic/hadronic phase [40]—cannot be excluded.

## VI. SUMMARY

We have presented new data on $\phi$ production in central Pb+Pb collisions obtained by the NA49 experiment at $20A$, $30A$, $40A$, $80A$, and $158A$ GeV beam energies. No indications of medium modifications of the $\phi$ meson mass or width were observed. The energy dependence of the production characteristics was studied by comparing them with measurements at AGS and RHIC energies. We find that at low SPS energy, the data can be understood in a hadronic reaction scenario; while at higher energies, hadronic models fail to reproduce the data. A statistical hadron gas model with undersaturation of strangeness gives a good description of the measured yields. This suggests that $\phi$ production is ruled by partonic degrees of freedom, consistent with the previously found indications for the onset of deconfinement at lower SPS energy.

### Acknowledgments

This work was supported by the U.S. Department of Energy Grant DE-FG03-97ER41020/A000, the Bundesministerium für Bildung und Forschung, Germany (06F137), the Polish State Committee for Scientific Research (2 P03B 006 30, SPB/CERN/P-03/Dz 446/2002-2004, 2 P03B 04123), the Hungarian Scientific Research Foundation (T032648, T032293, T043514), the Hungarian National Science Foundation, OTKA, (F034707), the Polish-German Foundation,

and the Korea Research Foundation Grant (KRF-2003-070-C00015).

[1] P. Koch, B. Müller, and J. Rafelski, Phys. Rep. **142**, 167 (1986).
[2] J. Bartke *et al.*, Z. Phys. C **48**, 191 (1990).
[3] F. Sikler (NA49 Collaboration), Nucl. Phys. **A661**, 45c (1999).
[4] J. Cleymans and K. Redlich, Phys. Rev. C **60**, 054908 (1999).
[5] P. Braun-Munzinger, I. Heppe, and J. Stachel, Phys. Lett. **B465**, 15 (1999).
[6] P. Braun-Munzinger, D. Magestro, K. Redlich, and J. Stachel, Phys. Lett. **B518**, 41 (2001).
[7] R. Averbeck, R. Holzmann, V. Metag, and R. S. Simon, Phys. Rev. C **67**, 024903 (2003).
[8] F. Becattini, J. Manninen, and M. Gaździcki, Phys. Rev. C **73**, 044905 (2006).
[9] R. Stock, Phys. Lett. **B456**, 277 (1999).
[10] P. Braun-Munzinger, J. Stachel, and C. Wetterich, Phys. Lett. **B596**, 61 (2004).
[11] R. Hagedorn and K. Redlich, Z. Phys. C **27**, 541 (1985).
[12] J. Rafelski and M. Danos, Phys. Lett. **B97**, 279 (1980).
[13] F. Becattini and U. Heinz, Z. Phys. C **76**, 269 (1997).
[14] P. Braun-Munzinger, J. Cleymans, H. Oeschler, and K. Redlich, Nucl. Phys. **A697**, 902 (2002).
[15] M. Gaździcki (NA49 Collaboration), J. Phys. G **30**, S701 (2004).
[16] V. Friese (NA49 Collaboration), J. Phys. G **31**, S911 (2005).
[17] M. Bleicher *et al.*, J. Phys. G **25**, 1859 (1999).
[18] M. Gaździcki and M. Gorenstein, Acta Phys. Pol. B **30**, 2705 (1999).
[19] S. C. Johnson, B. V. Jacak, and A. Drees, Eur. Phys. J. C **18**, 645 (2001).
[20] T. Hatsuda and S. Lee, Phys. Rev. C **46**, R34 (1992).
[21] D. Lissauer and E. V. Shuryak, Phys. Lett. **B253**, 15 (1991).
[22] R. Muto *et al.*, Phys. Rev. Lett. **98**, 042501 (2007).
[23] S. Afanasiev *et al.*, Phys. Lett. **B491**, 59 (2000).
[24] B. Alessandro *et al.*, Phys. Lett. **B555**, 147 (2003).
[25] D. Adamová *et al.*, Phys. Rev. Lett **96**, 152301 (2006).
[26] A. de Falco *et al.*, Nucl. Phys. **A774**, 719 (2006).
[27] B. B. Back *et al.*, Phys. Rev. C **69**, 054901 (2004).
[28] C. Adler *et al.*, Phys. Rev. C **65**, 041901(R) (2002).
[29] J. Adams *et al.*, Phys. Lett. **B612**, 181 (2005).
[30] S. S. Adler *et al.*, Phys. Rev. C **72**, 014903 (2005),
[31] S. Afanasiev *et al.*, Nucl. Instr. Methods Phys. Res.. A **430**, 210 (1999).
[32] D. Drijard and H. G. Fischer, Nucl. Instr. Methods Phys. Res. A **225**, 367 (1984).
[33] V. Friese, Dissertation, Universität Marburg 1999, `https://edms.cern.ch/document/816025/1`.
[34] R. Lednicki, private communication.
[35] J. D. Jackson, Nuovo Cimento **34**, 1644 (1964).
[36] S. Eidelmann *et al.*, Phys. Lett. **B592**, 1 (2004).
[37] A. Andronic, P. Braun-Munzinger, and J. Stachel, Nucl. Phys. **A772**, 167 (2006) 167; data provided by A. Andronic.
[38] S. V. Afanasiev *et al.*, Phys. Rev. C **66**, 054902 (2002).
[39] C. Alt *et al.*, Phys. Rev. C **77**, 024903 (2008).
[40] M. Gorenstein, M. Gaździcki, and K. Bugaev, Phys. Lett. **B567**, 175 (2003).